

# Numerical Study of the Passive Motion of Airfoils in Porous Media

J. Tang<sup>1</sup>, Z. Zhou<sup>1</sup>, Y. Zhang<sup>2,3</sup>, B. Moghtaderi<sup>3</sup> and Y. Wang<sup>1†</sup>

<sup>1</sup> School of Energy and Power Engineering, University of Shanghai for Science and Technology, Shanghai 200093, China

<sup>2</sup> National Engineering Laboratory for Pipeline Safety, MOE Key Laboratory of Petroleum Engineering, Beijing Key Laboratory of Urban Oil and Gas Distribution Technology, China University of Petroleum-Beijing, Beijing 102249, China

<sup>3</sup> Centre for Innovative Energy Technologies, The University of Newcastle, Callaghan, NSW 2308, Australia

†Corresponding Author Email: [wangying@usst.edu.cn](mailto:wangying@usst.edu.cn)

## ABSTRACT

This study proposes adding a porous medium layer to the leading edge of a rigid airfoil and investigates the influence of various porous medium properties on the passive propulsion performance of the airfoil in a Kármán vortex street, using numerical simulation methods. By employing a control variable approach, the study compares the force and motion characteristics of airfoils with nine different porosities and permeabilities under both the incoming flow mode and Kármán vortex street conditions. Porosity ( $\varepsilon$ ) is a parameter that describes the fraction of void volume relative to the total volume in a porous medium, ranging from  $\varepsilon=0.2$  to  $\varepsilon=0.92$ . This parameter determines the ability of fluid to penetrate the medium, with higher porosity allowing more fluid flow, thus significantly affecting the flow field structure. Permeability ( $\alpha$ ), ranging from  $10^{-12} \text{ m}^2$  to  $10^{-8} \text{ m}^2$ , indicates the ease with which fluid can pass through the porous medium and is a key factor in determining the flow resistance. Both porosity and permeability play crucial roles in the flow field and aerodynamic performance of the airfoil, and their interaction jointly regulates the formation of flow patterns and propulsion efficiency. The results show that under the incoming flow mode, the porous medium can significantly reduce the drag on the airfoil, with lower permeability leading to smaller aerodynamic forces. For high-permeability airfoils, drag reduction can be further achieved by lowering the porosity. In the Kármán vortex street, as both porosity and permeability decrease, the airfoil experiences reduced thrust, with an increase in horizontal displacement and a decrease in lateral deviation after release. This study deepens the understanding of passive propulsion phenomena in natural Kármán vortex streets and provides theoretical guidance and technical recommendations for related engineering applications.

## Article History

Received November 26, 2024

Revised March 2, 2025

Accepted March 8, 2025

Available online June 3, 2025

## Keywords:

*Porous media*

*Airfoil*

*Kármán vortex street*

*Passive motion*

*Numerical simulation*

## 1. INTRODUCTION

In nature, many organisms utilize energy from their surrounding environment for passive propulsion, thereby conserving energy and enhancing locomotion efficiency. Fish are able to swim upstream in turbulent currents without exerting physical effort by exploiting Kármán vortices formed behind reefs. This phenomenon demonstrates that the interaction between fluids and objects can significantly affect the motion state of the object, particularly in complex flow fields. When the surface of an object possesses specific structures or material properties, this interaction can be manipulated, enabling passive flow control and increasing movement efficiency. Similarly, airfoils are also affected by passive propulsion and Kármán vortex streets, where the interaction of surface structure, material properties, and the characteristic of the surrounding fluid plays a vital role

in determining the motion state and efficiency of the airfoil.

Porous media, also known as porous materials, are solid materials characterized by a pore structure (Bejan, 1995; Li, 2003) and they have recently emerged as significant subjects of research in the fields of flow control and passive propulsion. Porous media can modulate the pressure distribution and vortex formation of fluids by altering the flow structure over an airfoil's surface, thereby influencing the lift and drag characteristics of the airfoil. By optimizing parameters such as porosity, pore shape, and the distribution of the porous media, it is possible to effectively control the performance of the airfoil in complex flow fields, such as turbulence or Kármán vortex streets, thereby achieving more efficient passive propulsion. The incorporation of porous media is a typical passive flow control technique (Zamponi et al., 2020). Flow control technologies are generally classified into active and passive flow control

methods based on whether they require energy input (Kral, 2000). Minale (2018) indicates that the influence of the porous medium on vortex shedding stability is mainly reflected in the following aspects: (1) By altering the flow field structure, it can suppress or enhance vortex shedding. The presence of the porous medium introduces additional resistance and flow diffusion effects in the Kármán vortex street, thereby altering the frequency and intensity of vortex shedding. When the permeability is high, fluid can more easily penetrate the porous medium, which may weaken the vortex shedding characteristics. On the other hand, when the porosity is low, the porous medium may exacerbate the local flow instability. (2) Effect on vortex energy dissipation: The porous medium influences the energy transfer and diffusion of vortex shedding by increasing shear forces and turbulent dissipation. This effect is particularly pronounced under low permeability conditions. The combined effects of permeability and porosity jointly exert a comprehensive influence on vortex shedding characteristics by affecting the drag coefficient.

Porous media can effectively alter flow field characteristics, thereby controlling the development of the flow field, making the application of porous media on blunt body surfaces an effective passive control strategy. Zhang et al. (2024) demonstrated that the application of porous media significantly regulates the flow characteristics of a cylinder in crossflow by altering the timing of vortex shedding, the shear layer thickness, and the fluid recirculation behavior. Ruck et al. (2012) found that the leeward side of porous coatings can significantly reduce flow resistance by decreasing the recirculation velocity of the wake and the negative pressure, whereas full-surface coatings tend to increase resistance. Numerical studies by Naito and Fukagata (2012) indicated that porous surfaces significantly suppress velocity and pressure fluctuations through slip velocity and energy dissipation mechanisms, with the suppression effect intensifying as the Reynolds number increases. This effect particularly achieves complete suppression of vortex shedding at  $Re = 1.0 \times 10^5$ , showcasing potential for flow stability and turbulence control. Experimental results from Klausmann and Ruck (2017) revealed that leeward porous coatings significantly reduced the drag and oscillation amplitude of the cylinder by increasing base pressure and decreasing wake pressure fluctuations, with a maximum drag reduction of 13.2%. Wei et al. (2016) conducted wind tunnel experiments to study the influence of porous medium walls on cylindrical surfaces. The results showed that the porous medium wall reduced the velocity fluctuations and Reynolds stresses in the wake region, weakened the instability of the shear layer, and extended the vortex formation length.

Liu et al. (2022) conducted numerical simulations after treating the surfaces of two-dimensional airfoil trailing edges as porous media. They discovered that, at higher Reynolds numbers and low angle of attack, airflow could traverse the porous medium domain, forming recirculation structures within it. As the angle of attack increased, the airflow tended to move from the pressure side to the suction side due to the pressure differential between the upper and lower surfaces. Li et al. (2025) studied the NACA0012 airfoil by covering its surface with porous materials to simulate bird wing feathers. They found that the semi-covered porous airfoil could significantly improve aerodynamic performance,

particularly enhancing the airfoil's stall characteristics. Jiang (2021) investigated the characteristics of the vortex flow field, as well as variations in drag and lift around a cylinder with externally attached porous media at different porosities. Their results revealed that both the lift-to-drag ratio and the amplitude of fluctuations were markedly reduced. The porous medium suppressed the large-scale vortex shedding from the cylinder, decreasing the shedding frequency. Research by Yang et al. (2022) indicated that the presence of porous media could alter the lift and drag characteristics of the airfoil. While excessively thin porous media could degrade aerodynamic performance, an appropriate thickness could help balance aerodynamic performance and noise reduction effects. Feng et al. (2020) demonstrated that the porous medium trailing edge, driven by the pressure differential between the upper and lower surfaces, effectively mitigated fluctuations in aerodynamic loads on the airfoil surface. High-flow-resistance porous materials significantly reduced pressure pulsations on the airfoil surface, with trailing edge pressure fluctuations decreasing by over 20%, while low-flow-resistance materials exhibited a weaker effect.

The application of different porous media significantly influences the drag reduction effect on cylindrical structures. Research conducted by Hu et al. (2020) demonstrates that porous coatings significantly affect vortex shedding and noise characteristics by adjusting the separation point location and the coverage of the coating. Analysis using POD and DMD methods revealed that the porous coating reduces drag by altering the energy distribution of dominant modes and enhancing the stability of the flow field. Aguiar et al. (2018) investigated four different laying angle schemes for porous media and found that applying porous media at a  $270^\circ$  angle on the windward side of the cylinder resulted in the most effective drag reduction control. These studies indicate that porous media enhances the slip velocity at the porous interface, thereby reducing the frequency of vortex shedding. Furthermore, research by Du et al. (2022) showed that, at a Reynolds number of  $5.6 \times 10^4$ , the drag reduction effect can reach 8.53% when porous media are applied at a  $270^\circ$  angle on the rear edge of the cylinder.

In previous research conducted by the research group (Zhou et al, 2023; Zhou & Wang 2024) flow regulation has been a key focus for achieving energy harvesting and optimizing fluid systems. Both flexible and rigid structures can significantly influence fluid dynamic performance through Kármán vortex streets. However, this study primarily investigates the effect of the porous medium on the regulation flow behavior and drag characteristics. By exploring the mechanisms through which porosity modulates the flow field, the performance of the porous medium in fluid systems can be further optimized. However, given the diverse morphologies of fish in nature, most studies have opted to investigate the NACA0016 airfoil, which resembles the shape of a trout. Currently, there is no evidence to suggest that the NACA0016 exhibits optimal passive motion performance within Kármán vortex flow fields. Therefore, it is essential to explore the motion mechanisms of various airfoil thicknesses based on the NACA0016 in different media within Kármán vortex streets, a process that has been examined in reference (Zhou et al., 2023). Additionally, due to the unique flow characteristics of porous media,

incorporating such materials around the airfoil may enhance its passive propulsion effectiveness. To date, there has been no research on the role of porous media in passive propulsion, opening a new avenue for investigation. Therefore, this study will introduce porous media structures to the surface of the original airfoil to explore their effects on passive propulsion, aiming to achieve more efficient energy acquisition and utilization within vortex flows. This research seeks to deepen our understanding of passive propulsion utilizing Kármán vortex streets in nature while providing new theoretical foundations and technical guidance for engineering applications.

## 2. RESEARCH SUBJECTS AND NUMERICAL METHODS

Based on previous research (Zikang & Wang 2024), preliminary observations indicate that porous media can enhance the horizontal movement distance of airfoils in passive propulsion to a certain extent. Building on this foundation, this study conducts simulation tests on nine different types of porous media. By comparing the flow field characteristics of the airfoil in the incoming flow field and the Kármán vortex street, as well as analyzing the passive motion of the airfoil after release, we explore the mechanisms through which porous media influence the motion performance of the airfoil.

### 2.1 Geometric Model Structure of the Counterflow Mode and Parameter Settings for Porous Media

The focus of this study is on two-dimensional (2D) numerical simulations to investigate the effect of the Kármán vortex street behind the column bypass on porous media airfoil. This study specifically focuses on the NACA0016 airfoil, for which numerical calculations of the airfoil model were conducted. A semi-circular cylinder was placed in the flow field, with the computational domain defined as  $-10D \leq x \leq 10D$ ,  $-10D \leq y \leq 10D$ , where  $D$  is the diameter of the semi-circular cylinder (the characteristic length). The top of the airfoil is set as the origin of the coordinate system, with the positive direction along the x-axis towards the semi-circular cylinder, and the distance between the airfoil and the cylinder is  $4D$ . The centroid of the airfoil is positioned  $0.3L$  from the leading edge, with a mass of 0.01kg. The airfoil length is  $L=0.1\text{m}$ , and the cylinder diameter is  $D=0.05\text{m}$ . The left boundary is defined as a velocity inlet with a semicircular shape, while the right boundary serves as a pressure outlet. The semi-circular cylinder and the surface of the airfoil are set as no-slip boundary conditions. The velocity is specified as  $U = 0.45 \text{ m/s}$ , directed along the positive x-axis. Air is chosen as the working fluid, with  $\rho = 1.225 \text{ kg/m}^3$  and  $\nu = 1.7894 \times 10^{-5} \text{ kg/s/m}$ . Based on the cylinder diameter  $D$ , the Reynolds number is  $Re=1540$ . The SST  $k-\omega$  turbulence model is employed, and a pressure-based solver suitable for low-speed incompressible flows is used. The discretization scheme for the momentum equation is set to QUICK format, while the pressure term is discretized using a second-order upwind scheme. For the unsteady discretization, a second-order implicit scheme is selected, and the pressure-velocity coupling is handled using the SIMPLEC method. It is assumed that the airfoil undergoes only passive motion after release; therefore, the 6DOF dynamic mesh model in Fluent is employed for

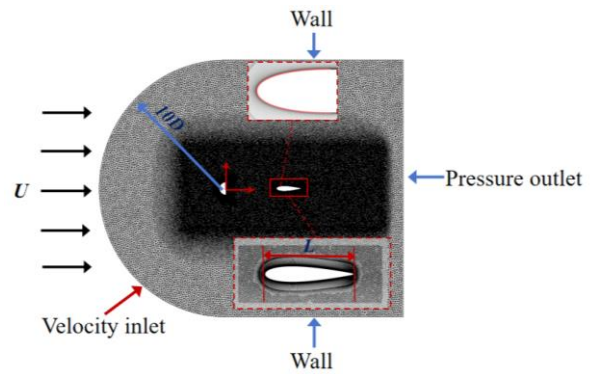


Fig. 1 Grid partitioning diagram

simulation.

To balance computational time and accuracy and ensure mesh movement and re-meshing during the passive motion of the airfoil, the computational domain is divided into blocks. Mesh refinement is applied to the regions where the flow is complex and varies significantly, ensuring that the first layer of mesh near the wall has a thickness smaller than the order of  $10^{-4}$ , keeping the  $y+$  value consistently below 1 to ensure computational accuracy. Unstructured meshes are used in the areas surrounding the semi-circular cylinder and the NACA airfoil. The airfoil's attached grid employs a first layer height of  $5 \times 10^{-5}$  to generate 10 layers with a growth rate of 1.0, thereby constructing the near-wall grid region. The outer side of the near-wall grid is generated with a growth rate of 1.1, resulting in 30 layers of grid. An area segmentation technique is applied to the near-wall grid at 30% of the airfoil's leading edge to delineate the porous region grid, as illustrated in Figure 1. The gray area surrounding the airfoil represents the fluid region, while the red area indicates the porous medium region. For clarity, the airfoil with the attached porous medium will be referred to as the "porous airfoil" in subsequent analyses.

To accommodate the distortion of the wall region grid during motion, a grid overlapping technique is employed to facilitate the coordinated movement of the airfoil and the porous medium region grid. The foreground grid area is a rectangle measuring  $2L$  in length and  $0.6L$  in width, with the airfoil positioned at the center of this area. To minimize computational errors, the dimensions of the foreground grid edge in the overlapping region are kept consistent with those of the background grid, as shown in Fig 1. The grid used in the flow field tests in this chapter accounts for the impact phase of the incoming flow during the motion of the airfoil, and is based on the original grid, with the addition of a grid excluding the semi-circular cylindrical bodies. Porosity and permeability are key parameters that significantly influence the performance of porous media, and their values should be determined considering both fluid dynamics and structural stability. The recommended range for porosity is  $0.2 \leq \epsilon \leq 0.92$ . Below  $\epsilon=0.2$ , the void volume becomes too small, significantly reducing fluid permeability, and the material may even exhibit solid-like characteristics. According to literature (Bear, 1972; Nield & Bejan, 2006), when porosity exceeds 0.92, the permeability of the material approaches infinity,

**Table 1 Properties of porous medium materials**

Serial Number	Porosity $\varepsilon$	Permeability $a/m^2$	The coefficient of viscous resistance $D_{ij}/m^2$	Inertial resistance coefficient $C_2/m^{-1}$
1	0.92	$4.78 \times 10^{-7}$	$2.1 \times 10^6$	468.41
2	0.5	$4.78 \times 10^{-7}$	$2.1 \times 10^6$	1169.10
3	0.2	$4.78 \times 10^{-7}$	$2.1 \times 10^6$	4621.29
4	0.8	$4 \times 10^{-8}$	$2.5 \times 10^7$	1996.90
5	0.8	$4 \times 10^{-9}$	$2.5 \times 10^8$	6314.76
6	0.8	$4 \times 10^{-10}$	$2.5 \times 10^9$	19969.05
7	0.8	$4 \times 10^{-12}$	$2.5 \times 10^{11}$	199690.51
8	0.5	$4 \times 10^{-12}$	$2.5 \times 10^{11}$	404145.19
9	0.2	$4 \times 10^{-12}$	$2.5 \times 10^{11}$	1597524.13

effectively resembles a frictionless free flow. The recommended range for permeability is  $10^{-12} m^2 \leq a \leq 10^{-7} m^2$ . When permeability is below  $10^{-12} m^2$ , it becomes difficult for the fluid to penetrate the medium, and above  $10^{-7} m^2$ , the fluid resistance is too low, potentially compromising the ability to regulate the flow field. This study employs a controlled variable method to test nine different porous medium materials characterized by varying permeability and porosity, with specific material properties detailed in Table 1. The nine porous media are categorized into three groups for analysis: samples numbered 1 to 3 represent the high permeability with variable porosity group; samples numbered 4 to 7 correspond to the constant porosity with variable permeability group; and samples numbered 7 to 9 are classified as the low permeability with variable porosity group.

## 2.2 Flow Control Equations

### 1) Continuity Equation

In this research, the flow of water at low Reynolds numbers can be approximated as an incompressible fluid, allowing the two-dimensional continuity equation to be simplified as follows:

$$\frac{\partial u}{\partial x} + \frac{\partial v}{\partial y} = 0 \quad (1)$$

In fluid mechanics, the momentum equation is a fundamental conservation equation based on Newton's second law (ANSYS Inc, 2018). By applying Reynolds averaging to the instantaneous momentum equation, the Reynolds-averaged equations that govern turbulence are obtained. The momentum equation is the representation of the law of conservation of momentum in hydrodynamics:

$$\frac{\partial u}{\partial t} + u \frac{\partial u}{\partial x} + v \frac{\partial u}{\partial y} = -\frac{1}{\rho} \frac{\partial p}{\partial x} + f_x + \mu \left( \frac{\partial^2 u}{\partial x^2} + \frac{\partial^2 u}{\partial y^2} \right) \quad (2)$$

$$\frac{\partial v}{\partial t} + u \frac{\partial v}{\partial x} + v \frac{\partial v}{\partial y} = -\frac{1}{\rho} \frac{\partial p}{\partial y} + f_y + \mu \left( \frac{\partial^2 v}{\partial x^2} + \frac{\partial^2 v}{\partial y^2} \right) \quad (3)$$

where:  $u$ ,  $v$ , and  $w$  are the three velocity components;  $p$  is the pressure;  $\rho$  is the fluid density; and  $\mu$  is the hydrodynamic viscosity. The convection term  $u \frac{\partial u}{\partial x} + v \frac{\partial u}{\partial y}$

reflects the contribution of the fluid velocity field to momentum transfer; the pressure gradient term  $\frac{1}{\rho} \frac{\partial p}{\partial x}$

represents the body force caused by the pressure distribution of the fluid; the body force term  $f_x$  indicates the external forces acting on a fluid element; the viscous term  $\mu \left( \frac{\partial^2 u}{\partial x^2} + \frac{\partial^2 u}{\partial y^2} \right)$  reflects the momentum diffusion due to the viscous effects within the fluid.

In the computational model, the inlet horizontal velocity is  $U=0.45m/s$ , and the cylinder diameter is  $D=0.05 m$ . The Reynolds number is the most important dimensionless parameter describing the motion of viscous fluids, and its physical significance characterizes the dimensionless similarity parameter between inertial and viscous forces.

$$Re = \rho v L / \mu \quad (4)$$

where:  $v$  and  $L$  are the characteristic velocity and characteristic length of the flow field, respectively.

### 2) Turbulence Models

The SST  $k-\omega$  model combines the advantages of both the  $k-\omega$  and  $k-\varepsilon$  models, exhibiting the following characteristics: (1) higher accuracy in predicting flow separation (Menter, 1994); (2) a good ability to capture flow characteristics in adverse pressure gradient regions (Spalart, 2000); (3) more accurate simulation of velocity gradients and vorticity variations in the wake region near the wall (Langtry & Menter, 2011). Therefore, the SST  $k-\omega$  turbulence model is used for numerical simulations in this study.

$$\frac{\partial}{\partial t}(\rho k) + \frac{\partial}{\partial x_i}(\rho k u_i) = \frac{\partial}{\partial x_i} \left( \Gamma_k \frac{\partial k}{\partial x_i} \right) + G_k - Y_k + S_k + G_b \quad (5)$$

$$\frac{\partial}{\partial t}(\rho \omega) + \frac{\partial}{\partial x_i}(\rho \omega u_i) = \frac{\partial}{\partial x_j} \left( \Gamma_\omega \frac{\partial \omega}{\partial x_j} \right) + G_\omega - Y_\omega + S_\omega + G_{\omega b} \quad (6)$$

where:  $k$  is the turbulent kinetic energy,  $\omega$  is the turbulent dissipation rate, and  $\Gamma$  is the effective diffusion coefficient,  $G_k$  denotes the turbulent kinetic energy production term due to the mean velocity gradient,  $G_\omega$  denotes the  $\omega$  production term,  $\Gamma_k$  and  $\Gamma_\omega$  denote the effective diffusion rate for  $k$  and  $\omega$ , respectively,  $Y_k$  and  $Y_\omega$  denote the dissipation of  $k$  and  $\omega$  due to turbulence,  $S_k$  and  $S_\omega$  are a user-defined source term,  $G_b$  and  $G_{\omega b}$  denote the buoyancy term.

### 3) Modelling of porous media

**Table 2 Comparison of each parameter of airfoil with different grids**

Grid Name	Grid number	$C_t$	$C_l$	$C_{l-1}$	$C_{l-1}$	y+	$\Delta y_{min}$
Grid-1	165201	0.01038	0.15931	-0.08039	0.03513	1	$5 \times 10^{-5}$
Grid-2	245154	0.01183	0.17671	-0.07695	0.03672	1	$5 \times 10^{-5}$
Grid-3	381897	0.01202	0.17947	-0.07626	0.03667	1	$5 \times 10^{-5}$
Grid-4	497690	0.01262	0.18224	-0.07618	0.03846	1	$5 \times 10^{-5}$

Porosity  $\varepsilon$  is the proportion of the void fraction in a porous medium that occupies the entire volume of the object.

$$\varepsilon = \frac{V}{V_0} \times 100\% \quad (7)$$

where:  $V$  is the pore volume.  $V_0$  is the total volume of the control body.

The permeability  $\alpha$  characterizes the ability of a fluid to flow through a porous medium.

$$\alpha = \frac{\varepsilon^3 D_p^2}{150(1-\varepsilon)^2} \quad (8)$$

where:  $D_p$  is the pore diameter.

The inertia drag coefficient refers to the ratio of the inertial drag in the porous medium to the acceleration, with the inertial drag being directly proportional to the acceleration of the cylinder. Most studies currently rely on experimental analysis methods. Empirical formulas are often used to describe it (Ergun & Orning 1949). For example, the commonly used inertia drag coefficient  $C_2$  can be expressed as follows:

$$C_2 = \frac{3.5(1-\varepsilon)}{D_p \varepsilon^3} \quad (9)$$

Assuming that the porous medium is simple isotropic, the porous medium is modelled by adding a source term to the standard  $N-S$  (Navier-Stokes) equation, which consists of two parts: a viscous loss term and an inertial loss term, as shown below (ANSYS Inc, 2018):

$$S_i = -\left( \sum_{j=1}^3 D_{ij} \mu v_j + \sum_{j=1}^3 C_{ij} \frac{1}{2} \rho |v_j| v_j \right) \quad (10)$$

where  $D_{ij}$  denotes the viscous loss term and  $C_{ij}$  denotes the inertial loss term. When it is isotropic, the equation can be simplified as.

$$S_i = \frac{\mu}{\alpha} v_i + C_2 \frac{1}{2} \rho |v_j| v_j \quad (11)$$

where:  $C_2$  represents the inertial resistance coefficient of the porous medium,  $\alpha$  is the permeability.

### 3) Calculation of relevant parameters

To investigate the forces and moments acting on the airfoil, this study defines the thrust coefficient  $C_t$  whose magnitude is equal to the drag coefficient  $C_d$  but with the opposite direction, as well as the definition of the lateral force coefficient  $C_l$ . The formulas are as follows:

$$C_t = \frac{-F_D}{0.5 \rho U^2 L} \quad (12)$$

$$C_l = \frac{F_L}{0.5 \rho U^2 L} \quad (13)$$

where:  $F_D$  is the drag force parallel to the fluid flow, with the direction aligned with fluid flow direction. The direction of  $C_t$  is opposite to the direction of fluid flow directions, representing the magnitude of the vortex street traction force.  $F_L$  is the lateral force perpendicular to the direction of the fluid flow.

### 2.3 Verification of Grid Independence and Time Step Independence

The airfoil used is the NACA0016 profile, and four distinct grids were generated, designated as Grid-1, Grid-2, Grid-3, and Grid-4. The computations continued until the Kármán vortex street stabilized and exerted periodic forces on the airfoil. The extreme values of the airfoil's lift coefficient ( $C_l$ ) and thrust coefficient ( $C_t$ ) were recorded alongside those of the semi-circular cylinder ( $C_{l-1}$ ,  $C_{t-1}$ ). The results are presented in Table 2. The relative difference in aerodynamic forces on the airfoil between Grid-2 and Grid-3 was found to be 1.58%, semi-circular cylinder force error of 0.91%. For subsequent calculations, Grid-2 was selected as the computational grid, considering computational efficiency. Additionally, the Strouhal number ( $S_t$ ), an auxiliary metric used to describe periodic unsteady flows in fluid dynamics, was employed to evaluate the grid. Roshko (1954) conducted extensive experimental studies on the flow around cylinders and proposed an empirical formula for calculating  $S_t$  for  $Re > 300$ :

$$S_t = 0.212 \times (1 - 12.7/R_e) \quad (14)$$

$$300 < R_e < 10000$$

The relative errors of  $C_t$  compared to  $C_{t-1}$  are 2.70% and 1.69%, while the relative errors of  $C_l$  compared to  $C_{l-1}$  are 1.36% and 3.94%. For time steps of 0.0005 s and 0.001 s, the relative errors of  $C_t$  compared to  $C_{t-1}$  are 2.96% and 2.86%, and the relative errors of  $C_l$  compared to  $C_{l-1}$  are 0.42% and 0.08%. To ensure accuracy and optimize computational time, a time step of 0.001 s has been selected for subsequent research.

To ensure the accuracy of both the simulation process and the results, a comparison was made between the simulation outcomes and the empirical formulas of Roshko (1954), as well as the experimental results of Peng (2012) and Igarashi (1982), within the range of  $Re = 1000$  to  $3000$ . The computed results, as illustrated in Fig. 2, demonstrate a strong correlation between the simulation results for  $St$  numbers in the  $Re = 1000$  to  $3000$  range and the empirical formulas and experimental data, with an error margin of less than 3%.

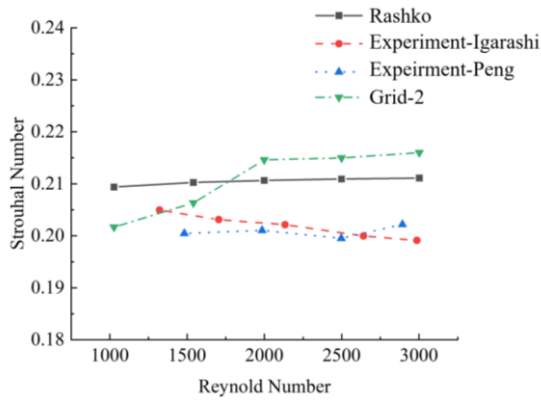


**Fig. 2 Validation of numerical methods based on the Strouhal number**

### 3. CALCULATION RESULTS AND ANALYSIS

#### 3.1 Calculation Results of Welcoming Flow

A simulation was conducted on the flow pattern around a non-half cylindrical structure. During the simulation, the incoming flow directly impacted the porous airfoil, and the airfoil was released once the flow field reached a stable state. Taking the NACA0016 as an example, Fig. 3 illustrates the lift forces of a smooth airfoil compared to various porous airfoils under the incoming flow condition. When the airfoil is subjected to the incoming flow, it primarily experiences drag, resulting in a negative lift force. Compared to smooth airfoils, porous airfoils generally exhibit reduced drag. Under conditions of high permeability, decreasing porosity leads to a reduction in drag experienced by the airfoil. At constant porosity, reducing permeability also decreases the drag on the airfoil. However, at low permeability, reducing porosity does not decrease the drag on the airfoil and may even lead to an increase in drag. As both porosity and permeability decrease, the porous medium transitions towards a solid state, resulting in diminished interactions the incoming flow on the airfoil surface. As the solid characteristics of the porous medium further increase, the portion of the porous medium exposed to the incoming flow impact intensifies, transmitting this force to the airfoil surface. Consequently, at low permeability, the drag experienced by the airfoil increases as porosity decreases.

According to the Darcy-Forchheimer model equation (Whitaker, 1996), as permeability decreases, viscous resistance increases significantly. In this case, the fluid resistance is mainly dominated by the viscous effect, and the inertial term gradually loses its influence. As porosity is further reduced, the fluid resistance tends to behave more like solid-to-fluid resistance. Specifically, lower permeability increases the fluid's adhesion, reducing flow separation and thus decreasing the pressure drag caused by separation. When permeability is low, the flow through the porous medium becomes more controlled, and the boundary layer is less prone to breakdown, which helps reduce vortex formation and wake formation, thereby lowering drag.

Figure 4 illustrates the variations in coordinates and

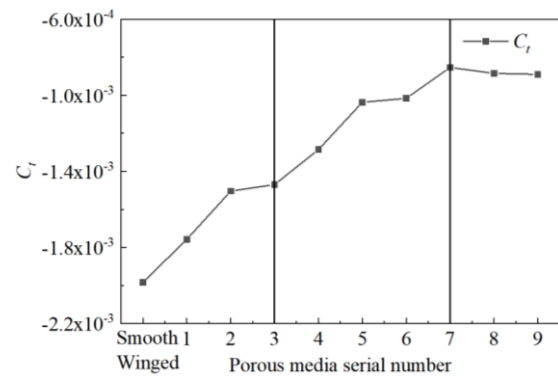


**Fig. 3 NACA0016 traction of various porous wing types**

smooth airfoil type after the release of degrees of freedom in an incoming flow pattern. The release duration is set to 1s, with a computational time step of 0.001s, resulting in a total of 1000 computational steps. After release, the airfoils experience backward motion due to drag effects, with the x-direction coordinate changes represented as absolute values in the figure. As shown in Fig. 4(a), although the porous airfoils experience less drags in a fixed state, their retreat speed after release is greater than that of the smooth airfoil. As permeability decreases, the retreat distance of the airfoils gradually diminishes, and at  $\alpha=4 \times 10^{-12}$ , the displacement distances of the porous and smooth airfoils become nearly identical. At a high permeability of  $\alpha=4.78 \times 10^{-7}$ , reducing porosity results in a decrease in the retreat distance of the airfoil; however, at a low permeability of  $\alpha=4 \times 10^{-12}$ , changes in porosity have minimal effect on the retreat distance. Figure 4(b) depicts the vertical displacement changes of the airfoils. After release, the airfoils exhibit slight vertical displacements. Overall, airfoils with high porosity demonstrate smaller lateral displacement amplitudes. Figure 4(c) presents the changes in attitude angles of the airfoils; under the incoming flow pattern, the amplitude of attitude angle variation is small, with the range of change for the porous airfoils being smaller than that of the smooth airfoil. However, at  $\alpha=4 \times 10^{-12}$ , a significant deflection occurs 0.2s after release, attributed to the low permeability disrupting the normal flow field, thereby affecting the attitude angle of the airfoil. As illustrated in Fig. 5, at  $\alpha=4 \times 10^{-12}$ , the vorticity in the porous medium region of the airfoil is obstructed by the external flow field, while at  $\alpha=4 \times 10^{-8}$ , the vorticity cloud distribution in the porous medium region is relatively uniform.

#### 3.2 Kármán Vortex Calculations

This chapter presents simulation calculations on various types of porous media using the NACA0016 airfoil. Figure 6 illustrates the vorticity contours of three types of porous media with  $\varepsilon=0.8$  at  $C_{l, max}$ . The permeability of the porous media decreases progressively from (a) to (c), resulting in the upstream vortices transitioning from direct contact with the airfoil surface to being completely obstructed by the porous airfoil. When the permeability is high, the fluid can penetrate the porous medium, inducing stronger fluid exchange and shear forces, which leading to the generation and stability of upstream vortices. As permeability decreases, the resistance of the porous medium to fluid penetration

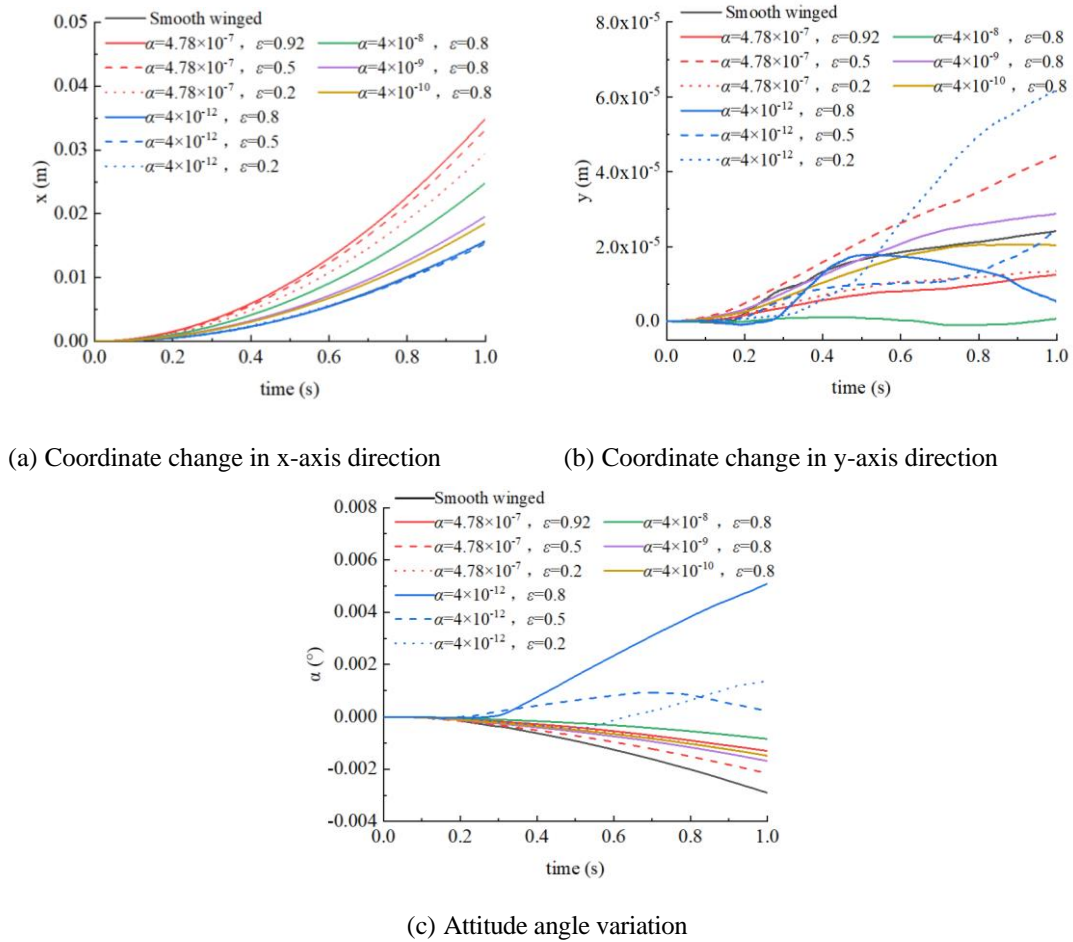


**Fig. 4** Variation of coordinates and attitude angle of various porous airfoils for NACA0016 in incoming flow condition

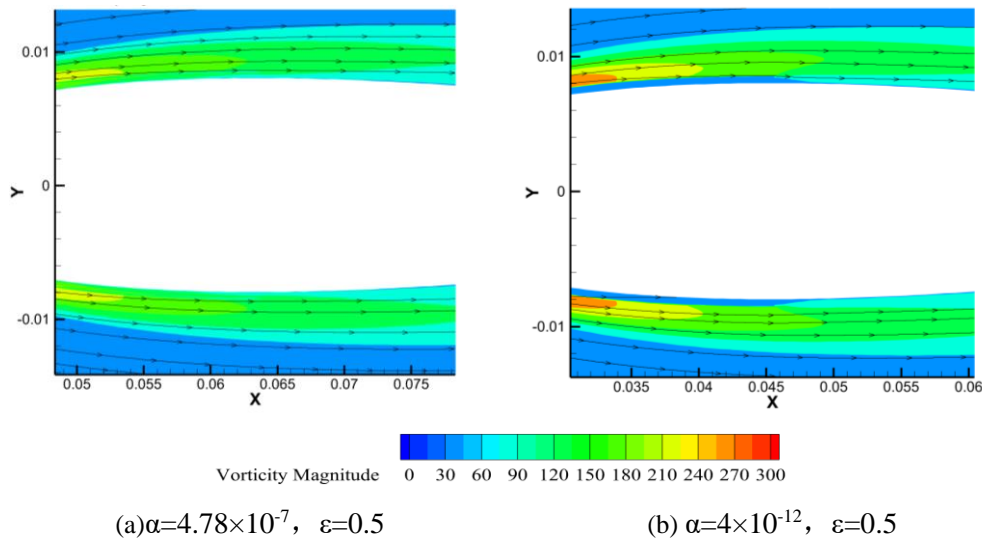


**Fig. 5** Vortex cloud and streamline diagrams of two porous airfoil types

increases, weakening the diffusion effects of the flow. The shear forces become insufficient to maintain a stable vortex structure, and the vortices gradually weaken until they completely vanish. Under low permeability conditions, the flow paths inside the porous medium become more complex, and local flow recirculation increases. This behavior may enhance turbulence

dissipation, thereby suppressing the generation and development of vortices. When the permeability is high (e.g.,  $\alpha=4 \times 10^{-8}$ ), the presence of upstream vortices enhances the pressure gradient at the leading edge of the airfoil, thereby increasing lift. As the vortices gradually weaken and disappear (e.g.,  $\alpha=4 \times 10^{-10}$ ), the pressure gradient on the airfoil surface decreases, leading to a

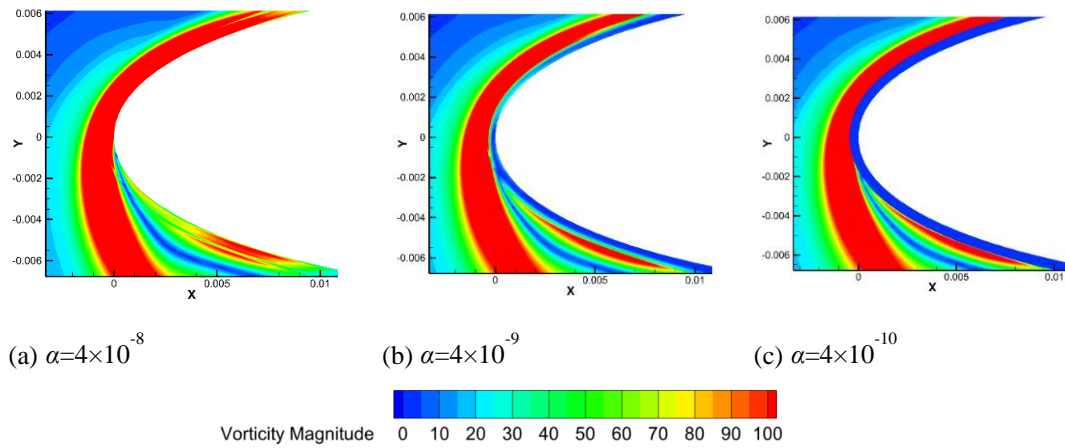


**Fig. 6** Leading edge vorticity plots at  $C_{t, max}$  for three airfoils with  $\varepsilon = 0.8$  porous media

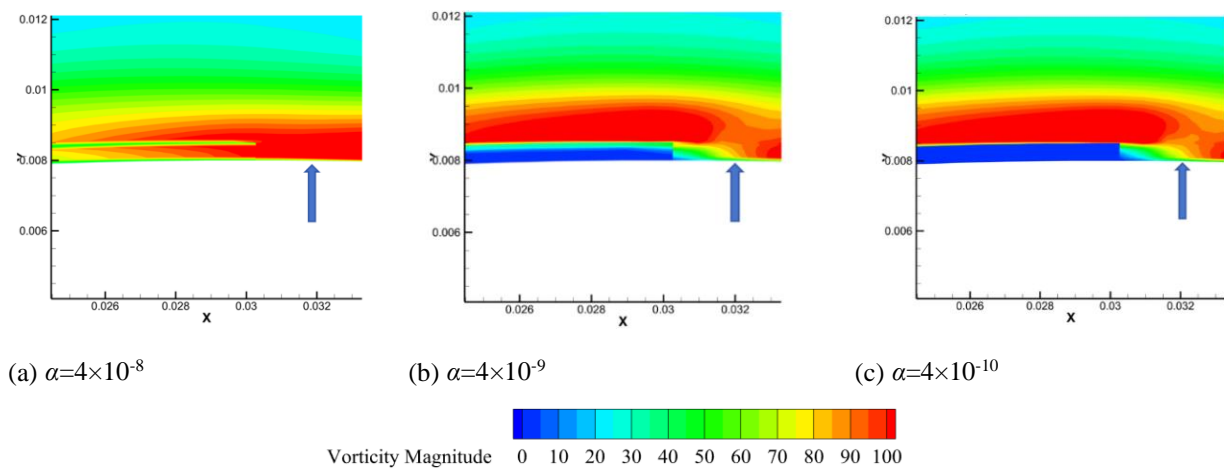


**Fig. 7** Plots of vorticity at the end of the porous region at  $C_{t, max}$  for three airfoils with  $\varepsilon = 0.8$  porous media

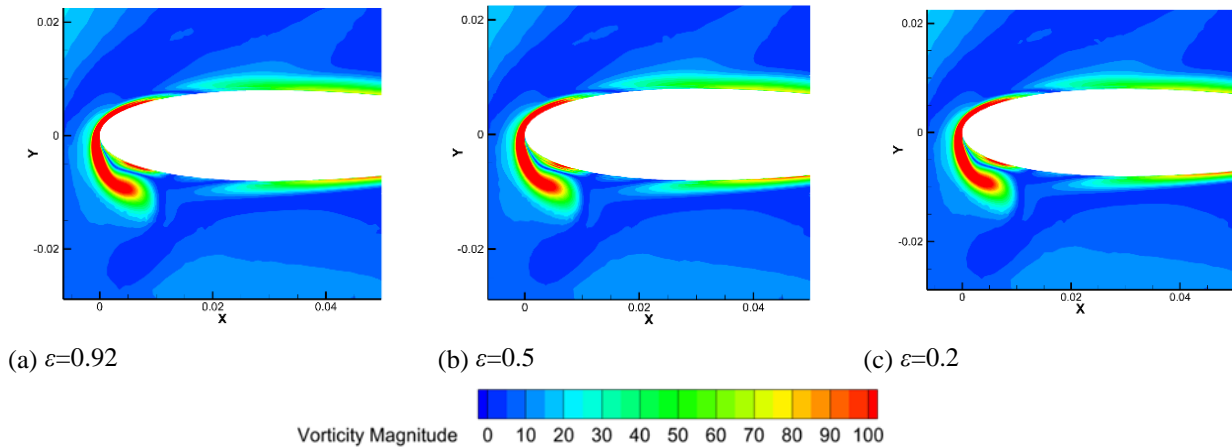
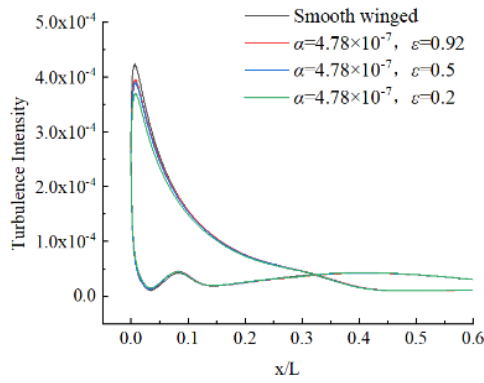


**Fig. 8** Vortex profiles at the leading edge of the airfoil at  $C_{t, max}$  for three  $\alpha = 4.78 \times 10^{-7}$  porous media

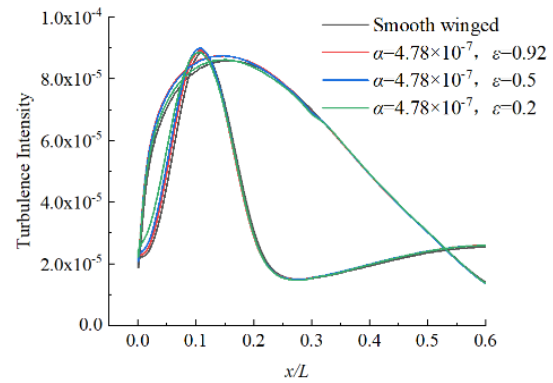
reduction in lift. Under high permeability conditions, the vortices can induce greater flow separation and turbulence intensity, increasing surface drag, which is consistent with the results in the literature (Smith, 1975).

Figure 7 illustrates the vorticity contours at the trailing edge of the porous regions for the three porous airfoils with  $\varepsilon=0.8$ . When permeability is high, the vorticity within the porous medium is continuous and maintains a consistent strength with external vorticity. As

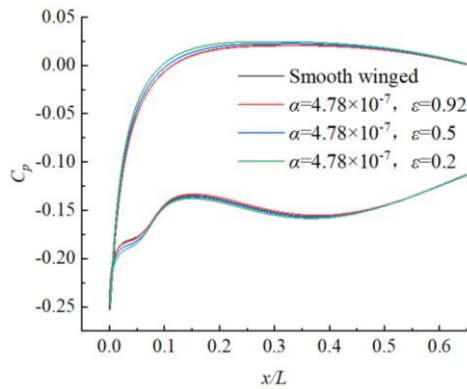
permeability decreases, the vorticity within the porous region gradually diminishes, ultimately reaching zero at the airfoil's surface, resulting in a "step-like" region of zero vorticity. This leads to an upward shift of the originally high vorticity area and progressively causes the vorticity region on the airfoil surface to break apart (as indicated by the arrows in Fig. 7). However, altering the porosity does not significantly affect the vorticity distribution within the porous medium. As shown in Fig. 7 and 8, changes in porosity have a minimal impact on the



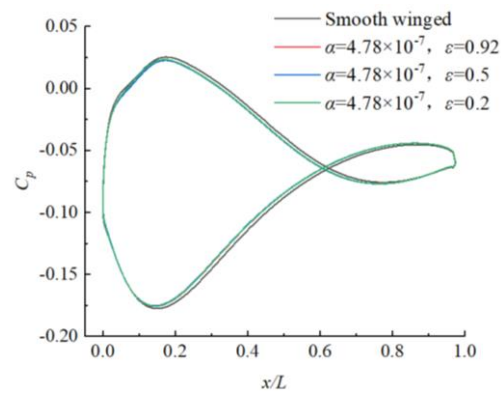
(a<sub>1</sub>) Turbulence intensity



(b<sub>1</sub>) Turbulence intensity



(a<sub>2</sub>) Surface pressure coefficient



(b<sub>2</sub>) Surface pressure coefficient

(a)  $C_{t, \max}$

(b)  $C_{t, \min}$

**Fig. 9 Airfoil turbulence intensity and surface pressure coefficients for three  $\alpha = 4.78 \times 10^{-7}$  porous media**

development of vortices within the porous medium, with the vortex strength remaining nearly unchanged.

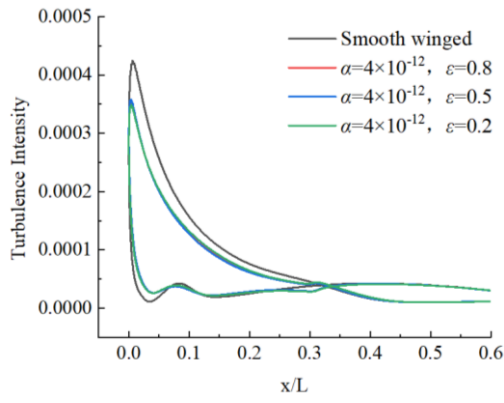
Figure 9 illustrates the trends in surface turbulence intensity and surface pressure coefficient following changes in porosity for high permeability porous media. As porosity decreases, the maximum turbulence intensity at the  $C_{t, \max}$  moment at the leading edge of the porous airfoil decreases, resulting in a corresponding reduction in the range of the turbulence intensity curve, while the range of the surface pressure coefficient curve expands. At the  $C_{t, \min}$  moment, the turbulence intensity curve exhibits a slight decrease at the end of the porous medium (at  $x/L=0.3$ ), which is hypothesized to be due to the variations in porosity leading to a reduction in turbulence intensity at this location.

Figure 10 illustrates the variations in surface turbulence intensity and surface pressure coefficient for three porous airfoil types compared to a smooth airfoil under low permeability conditions. As porosity decreases, the porous medium transitions towards a solid state. Similar to the high permeability scenario, the surface turbulence intensity and surface pressure coefficient remain highly consistent at both time instances under low permeability, indicating that changes in porosity have little to no significant impact on these two parameters.

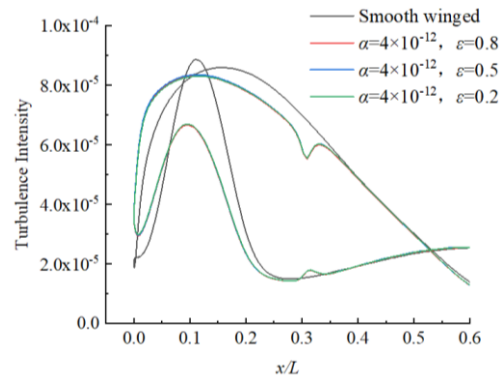
Figure 11 illustrates the extreme values of the drag coefficient for various porous media under the influence of the Kármán vortex street. Flow separation typically occurs when fluid flows around the surface of an object,

caused by changes in the pressure gradient that prevent the fluid from remaining attached to the surface. Additionally, an increase or decrease in boundary layer thickness can also lead to an increase or decrease in drag (Carotenuto and Minale, 2011). For porous airfoils with external porous media, the drag force is generally lower than that of smooth airfoils. Under high permeability conditions, a decrease in porosity results in a slight reduction in drag force. The boundary layer thickness decreases, the velocity gradient near the wall increases, and the fluid's adhesion to the surface strengthens, reducing fluid separation and thus lowering drag. When the porosity is low, fluid penetration through the porous medium is weakened, leading to a more stable surface flow field, which reduces the size of the separation region. The reduction in the separation region directly decreases both vortex drag and pressure difference drag. Conversely, when porosity remains constant, a reduction in permeability leads to a significant decrease in drag force. Under low permeability, a decrease in porosity only causes a minor reduction in drag force. These results indicate that permeability has a more substantial impact on the drag force of airfoils.

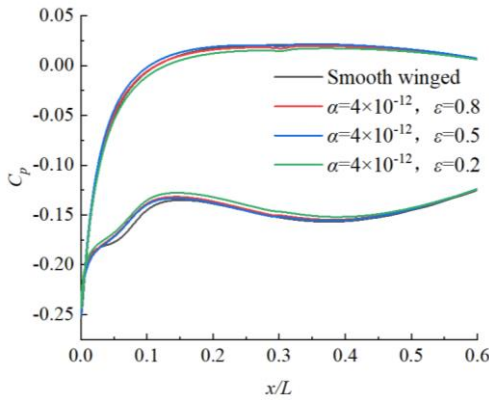
Figure 12 presents the horizontal displacement of porous airfoils with varying porosity. When the permeability of the porous medium is fixed, reducing porosity can increase the displacement of the porous airfoil. By comparing the slopes of the airfoil motion curves, it is evident that lower porosity correlates with higher airfoil velocity. Figure 13 depicts the vertical



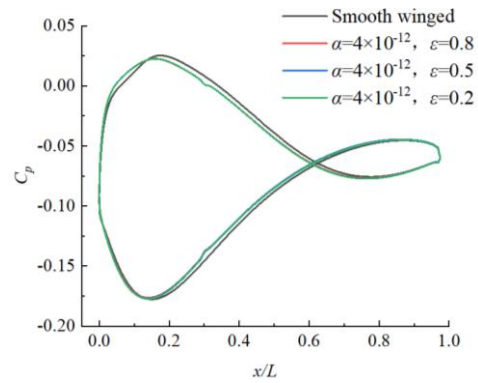
(a<sub>1</sub>) Turbulence intensity



(b<sub>1</sub>) Turbulence intensity



(a<sub>2</sub>) Surface pressure coefficient



(b<sub>2</sub>) Surface pressure coefficient

(a)  $C_{t, \max}$

(b)  $C_{t, \min}$

**Fig. 10 Turbulence intensity and surface pressure coefficients for three  $\alpha = 4 \times 10^{-12}$  porous media**

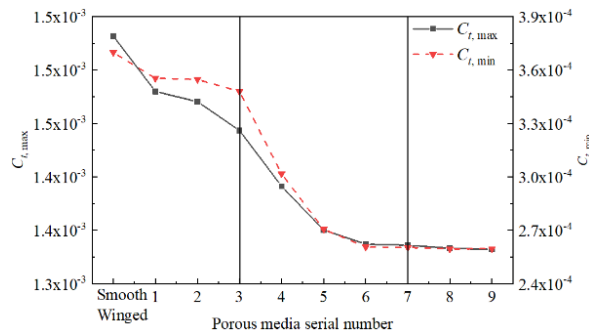
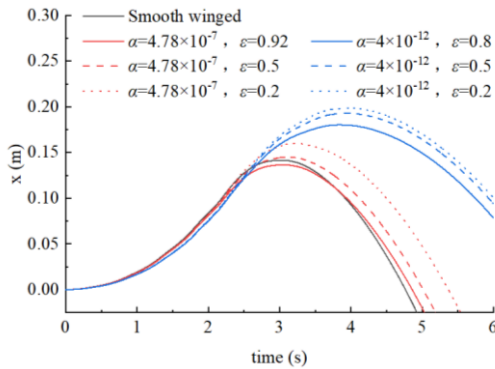
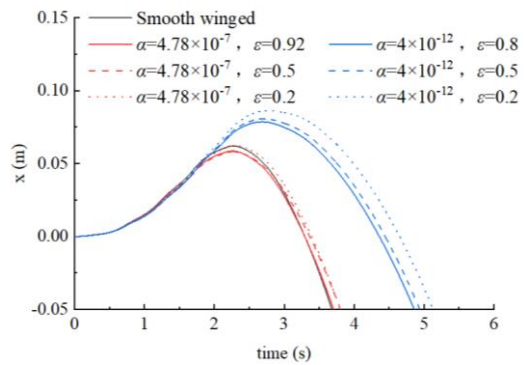


**Fig. 11 Maximum traction force of various porous media**

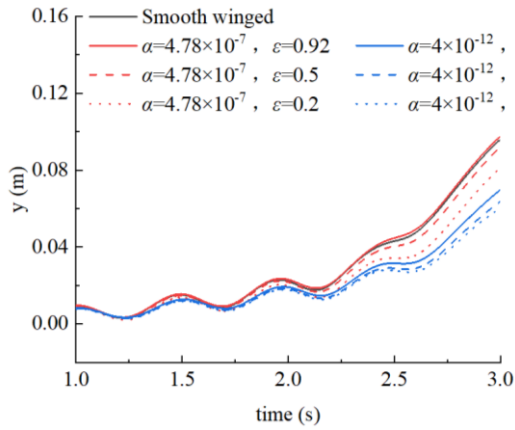


(a)  $C_{t, \max}$  release

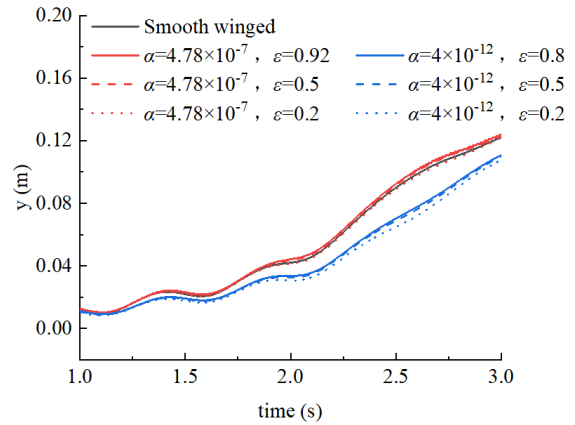


(b)  $C_{t, \min}$  release

**Fig. 12 Horizontal displacement of porous airfoil with variable porosity**

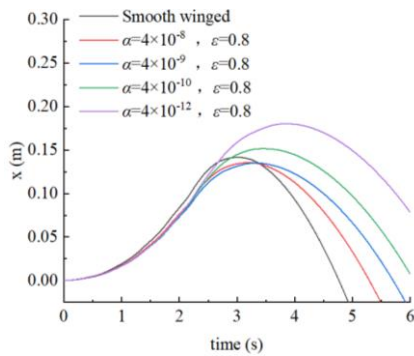


(a)  $C_{t, max}$  release

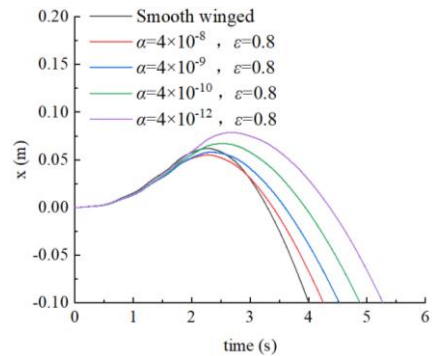


(b)  $C_{t, min}$  release

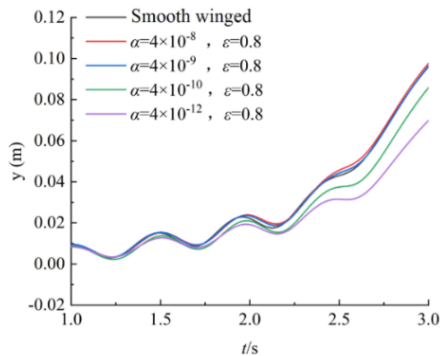
**Fig. 13 Vertical displacement of porous airfoil with variable porosity**



(a<sub>1</sub>) Coordinate change in x-axis direction

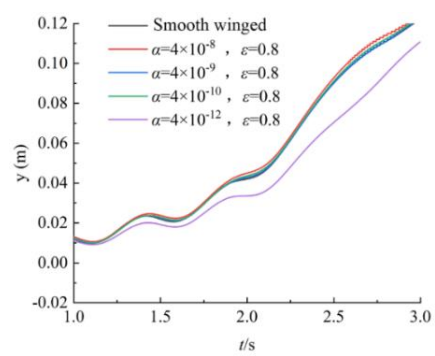


(b<sub>1</sub>) Coordinate change in x-axis direction



(a<sub>2</sub>) Coordinate change in y-axis direction

(a)  $C_{t, max}$  release



(b<sub>2</sub>) Coordinate change in y-axis direction

(b)  $C_{t, min}$  release

**Fig. 14 Variable permeability porous airfoil coordinate variation**

displacement of porous airfoils with varying porosity; as porosity decreases, the vertical displacement diminishes. Under high permeability conditions, changes in porosity have a more pronounced effect on vertical displacement. This study hypothesizes that, due to the high inertial resistance coefficient in low-permeability porous media, external fluids find it challenging to penetrate the internal porous regions, resulting in interactions primarily at the surface of the porous medium, which leads to a smaller magnitude of vertical variation.

Figure 14 illustrates the displacements of a porous airfoil in both horizontal and vertical directions with varying permeability. When the porosity of the porous medium is held constant, a reduction in permeability leads to an increase in the displacement of the porous airfoil. By comparing the slopes of the airfoil's motion curves, it is evident that lower permeability correlates with higher airfoil velocity. In the vertical direction, a decrease in the permeability of the porous medium can reduce airfoil's offset; however, significant changes in vertical displacement

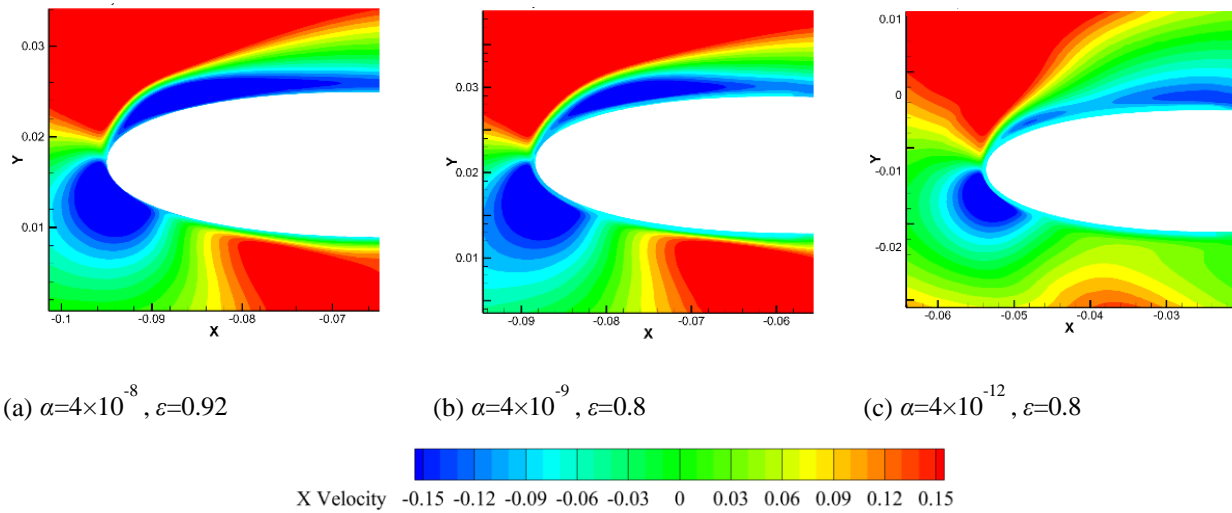


**Fig. 15 Horizontal velocity cloud for variable permeability porous airfoils**

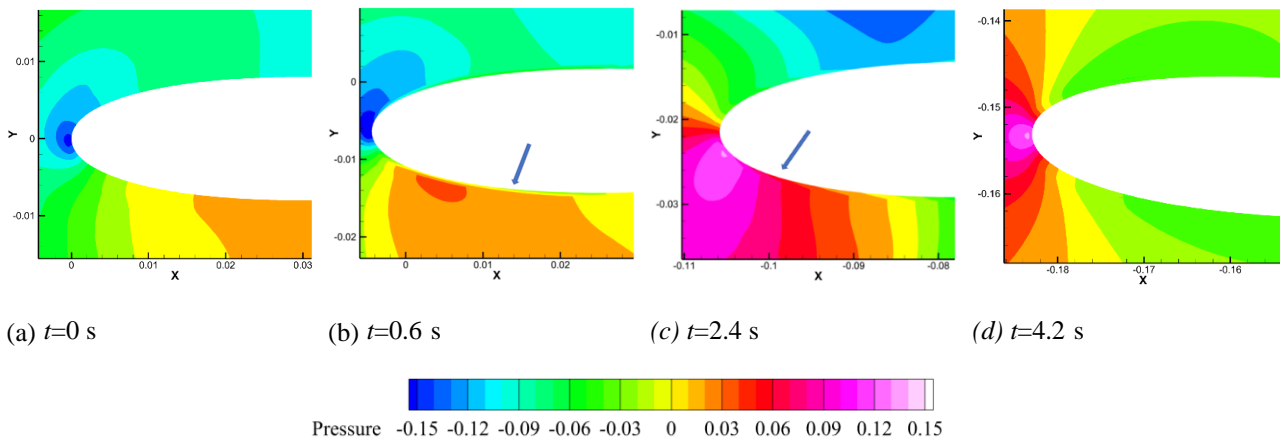


**Fig. 16 Pressure cloud during motion of porous airfoil ( $\alpha=4\times 10^{-12}$ ,  $\epsilon=0.8$ )**

only occur when the permeability is altered beyond a certain threshold. Notably, during the release of  $C_{t, \min}$ , a marked decrease in vertical offset is observed only when the permeability drops to  $\alpha=4\times 10^{-12}$ .

Figure 15 illustrates the horizontal velocity contour plots at  $t = 1.8$ s following the release of three types of porous airfoils. As shown in Fig. 16(a), the horizontal flow velocity of the fluid within the porous medium at the leading edge of the airfoil is comparable to the external flow velocity. However, as permeability decreases, a discrepancy arises between the fluid velocity near the airfoil surface within the porous medium and the velocity of the external flow field, as depicted in Fig. 16(b). Eventually, when the permeability is reduced to a certain extent, the flow velocity within the porous medium becomes uniform, completely segregating from the external velocity contour, as shown in Fig. 16(c). At this point, the fluid velocity within the porous medium matches the velocity of the airfoil's motion. Although the fluid within the porous region remains connected to the external fluid, the high inertial resistance coefficient of the low-permeability porous medium restricts the free movement of fluid in and out of the porous region, causing the fluid within this area to move at the same speed as the

airfoil.

Figure 16 presents the pressure contour within a porous medium ( $\alpha=4\times 10^{-12}$ ,  $\epsilon=0.8$ ) following the motion of a porous airfoil. Initially, when the airfoil is released (Fig. 16(a)), its velocity is zero, resulting in a continuous, coherent pressure contour both within and outside the porous medium. At this stage, the external pressure field enters the porous region in a "vertical" manner relative to the airfoil surface. However, as the airfoil encounters the Kármán vortex street, the pressure contour within the porous medium becomes discontinuous from the outflow field pressure contour (Fig. 16(b)). At the boundary of the porous medium, the external pressure field undergoes distortion to connect with the internal pressure field. The extent of this distortion is linked to the airfoil's velocity, reaching a peak as the airfoil attains its maximum displacement velocity (Fig. 16(c)), which coincides with the highest distortion of the surrounding pressure field. Once the airfoil moves away from the Kármán vortex street and loses its horizontal displacement velocity, returning to the incoming flow mode (Fig. 16(d)), the distortion in the pressure field decreases. This allows the external pressure field to once again enter the porous medium in a "vertical" manner. Figure 17 shows that

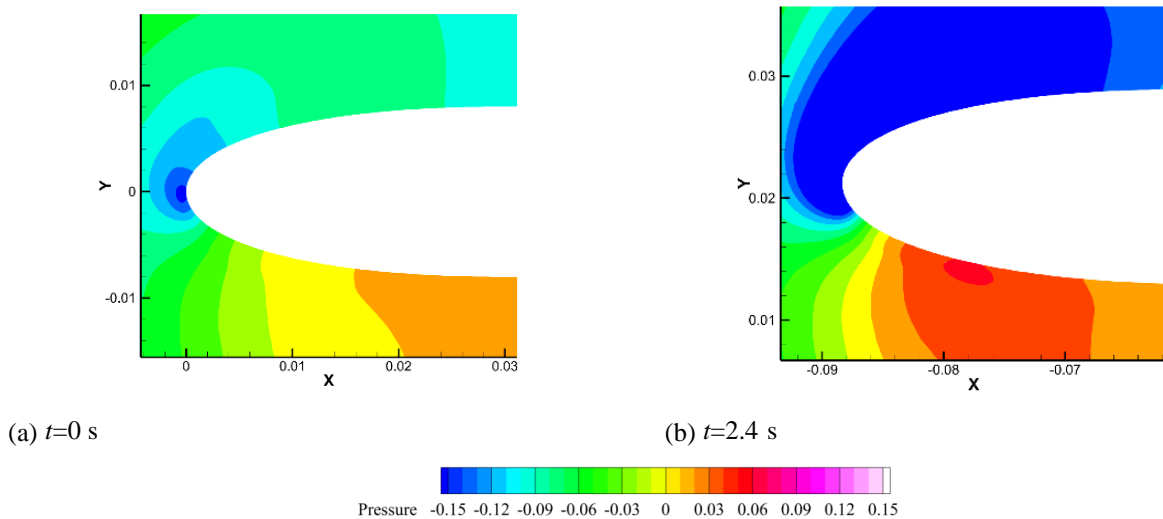


**Fig. 17** Pressure cloud during motion of porous airfoil ( $\alpha = 4 \times 10^{-9}$ ,  $\varepsilon = 0.8$ )

Under high-permeability conditions, the porous medium has minimal impact on pressure field distortion.

#### 4. CONCLUSION

This chapter employs the control variable method to test nine different porous media with varying porosities and permeabilities. It analyzes the impact of different porous media on the aerodynamic forces and motion of the porous airfoil under both Kármán vortex street and incoming flow conditions, drawing the following conclusions:

(1) Under incoming flow conditions, porous media can effectively reduce the drag on the airfoil. The lower the permeability of the porous medium, the smaller the drag acting on the airfoil. Additionally, decreasing porosity can further reduce the drag on high-permeability porous surfaces; however, this effect is less significant for low-permeability porous surfaces. Upon release, the airfoil moves backward, with the porous airfoil retreating more than the smooth airfoil. As permeability decreases, the backward motion of the airfoil diminishes, and the vertical displacement of the high-permeability airfoil is relatively smaller. By optimizing the permeability and porosity of porous airfoils, significant improvements can be made in the performance of vehicles, particularly in reducing drag during low-speed flight or steady states. For small aircraft or unmanned aerial vehicles, selecting a low permeability and appropriate porosity porous airfoil can enhance maneuverability and extend endurance, thereby improving overall efficiency.

(2) Under Kármán vortex street conditions, as permeability and porosity decrease, the lift acting on the airfoil also decreases. After release, reducing porosity can decrease the vertical displacement of the airfoil while increasing its horizontal displacement. Reducing permeability also increases horizontal displacement, but permeability must be reduced to a certain level to achieve a reduction in vertical displacement. By adjusting porosity and permeability appropriately, it is possible to reduce vertical displacement while increasing horizontal displacement, thus improving propulsion efficiency. In applications such as biomimetic fish or other propulsion

systems, optimizing these parameters can enhance lateral thrust, reduce energy consumption, and improve movement performance in complex flow environments.

#### ACKNOWLEDGMENTS

This study was sponsored by Shanghai Pujiang Program (Grant No. 23PJ1409500).

#### CONFLICT OF INTEREST

The authors have no conflicts to disclose.

#### AUTHORS CONTRIBUTION

**Jiawei Tang:** Investigation, Writing - Original Draft. **Zikang Zhou:** Methodology, Investigation Revision; **Yongxing Zhang:** Writing - Review & Editing; **Behdad Moghtaderi:** Writing - Review & Editing; **Ying Wang:** Conceptualization; Writing - Review & Editing; Supervision.

#### REFERENCES

- Aguiar, J., Birch, D. M., & Pelacci, M. (2018). *Wake vortex mechanisms behind semi-porous cylinders*. Proceedings of the 2018 Applied Aerodynamics Conference. <https://doi.org/10.2514/6.2018-3002>
- ANSYS Inc. (2018). ANSYS help 19.0: Fluent theory guide. Pennsylvania: ANSYS Inc.
- Bear, J. (1972). *Dynamics of fluids in porous media*. New York, NY: Dover Publications.
- Bejan, A. (1995). *Convection heat transfer* (2nd ed.). Wiley, New York.
- Carotenuto, C. & Minale, M. (2011). Shear flow over a porous layer: Velocity in the real proximity of the interface via rheological tests. *Physics of Fluids*, 23(6), 063102. <https://doi.org/10.1063/1.3601444>
- Du, H., Zhang, Q., He, L., Zhang, Y., Wang, S., & Liu, Y. (2022). Study on the characteristics and mechanism of cylindrical drag reduction in covered porous media.

- Journal of Nanjing University of Aeronautics and Astronautics*, 54(4), 611-622. <https://doi.org/10.16356/j.1005-2615.2022.04.008>.
- Ergun, S., & Orning, A. A. (1949). Fluid flow through randomly packed columns and fluidized beds. *Industrial and Engineering Chemistry*, 41(6), 1179-1184. <https://doi.org/10.1021/ie50474a011>
- Feng, H., Liu, Y., Wei, Z. Y., & Wang, Q. (2020). Numerical study of the effect of porous media on the wing-wound boundary layer. *Journal of Applied Mechanics*, 37(03), 1160-1165, 1397 (in Chinese)
- Hu, Z., Liu, H., Chen, N., & Hu, J. W. (2020). Vortex shedding noise and flow mode analysis of cylinder with full/partial porous coating. *Aerospace Science and Technology*, 106, 106154. <https://doi.org/10.1016/j.ast.2020.106154>.
- Igarashi, T. (1982). Flow characteristics around a circular cylinder with a slit: 2nd report, effect of boundary layer suction. *Bulletin of the Japan Society of Mechanical Engineers*, 25(207), 1389-1397. <https://doi.org/10.1299/jsme1958.25.1389>.
- Jiang, M. J. (2021). Study on the winding flow characteristics of structures with additional porous media. Harbin Engineering University. <https://doi.org/10.27060/d.cnki.ghbcu.2021.001539>
- Klausmann, K., & Ruck, B. (2017). Drag reduction of circular cylinders by porous coating on the leeward side, *Journal of Fluid Mechanics*, 813, 382-411. <https://doi.org/10.1017/jfm.2016.757>
- Kral, L. D. (2000). Active flow control technology. *ASME Fluids Engineering Technical Brief*, 1-28.
- Langtry, R. B., & Menter, F. R. (2006). A correlation-based transition model using local variables for unstructured parallelized CFD codes. *Journal of Turbomachinery*, 128(3), 423-434. <https://doi.org/10.1115/1.2184352>
- Li, C. L. (2003). Relationship between rock compression coefficient and porosity. *China Offshore Oil and Gas Geology*, (05), 65-8.
- Li, F., Hao, L., Bao, H., Zhang, Y., Wang, S., & Liu, Y. (2025). The influence of permeable characteristic parameters on the aerodynamic performance of airfoils. *Aerospace Engineering Progress*, 1-8. <http://kns.cnki.net/kcms/detail/61.1479.V.20241119.2341.002.html>
- Liu, J. Y. (2022). *Research on the suppression mechanism of porous media on aerodynamic noise of airfoil*. M.Sc. Thesis, Yangzhou University. <https://doi.org/10.27441/d.cnki.gyzdu.2022.001607>
- Minale, M. (2018). Polymer dynamics in porous media. In *Fluid mechanics of porous materials* (pp. 45-70). Springer. [https://doi.org/10.1007/978-3-319-50277-7\\_3](https://doi.org/10.1007/978-3-319-50277-7_3)
- Menter, F. (1994). Two equation eddy-viscosity turbulence modeling for engineering applications. *AIAA Journal*, 32, 1598-1605. <http://dx.doi.org/10.2514/3.12149>
- Naito, H., & Fukagata, K. (2012). Numerical simulation of flow around a circular cylinder having porous surface. *Physics of Fluids*, 24(11). <https://doi.org/10.1063/1.4767534>
- Nield, D. A., & Bejan, A. (2006). *Convection in porous media* (3rd ed.). New York, NY: Springer.
- Peng, B., Miao, J., Bao, F., Weng, L. D., Chao, C. C. & Hsu, C. C. (2012). Performance of vortex shedding from a circular cylinder with a slit normal to the stream. *Flow Measurement and Instrumentation*, 25, 54-62. <https://doi.org/10.1016/j.flowmeasinst.2011.07.003>
- Roshko, A. (1954). On the development of turbulent wakes from vortex streets. NACA Report No. 1191.
- Ruck, B., Klausmann, K., & Wacker, T. (2012). The flow around circular cylinders partially coated with porous media. *AIP Conference Proceedings* 1453(1), 49-54. <https://doi.org/10.1063/1.4711152>
- Smith, A. M. O. (1975). High-lift aerodynamics. *Annual Review of Fluid Mechanics*, 7(1), 179-218. <https://doi.org/10.2514/3.59830>
- Spalart, P. R. (2000). Strategies for turbulence modelling and simulations. *International Journal of Heat and Fluid Flow*, 21(3), 252-263. [https://doi.org/10.1016/S0142-727X\(00\)00007-2](https://doi.org/10.1016/S0142-727X(00)00007-2).
- Wei, Z., Yang, Z., Xia, C., Yuan, H., Li, Q., & Yang, Z. (2016). *Experimental study of the wake of a cylinder covered with porous media*. Proceedings of the Chinese Society of Astronautics; Chinese Society of Aerodynamics.
- Whitaker, S. (1996). The forchheimer equation: A theoretical development. *Transport in Porous Media*, 25(1), 27-50. <https://doi.org/10.1007/BF00141261>
- Yang, C. H, Feng, H. Y., & Peng, Y. H. (2022). Influence of porous media on cylindrical-wing interference noise. *Journal of Aerospace Dynamics*, 37(07), 1528-1538. <https://doi.org/10.13224/j.cnki.jasp.20210270>.
- Zamponi, R., Satcunanathan, S., Moreau, S., Ragni, D., & Meinke, M. (2020). On the role of turbulence distortion on leading-edge noise reduction by means of porosity. *Journal of Sound and Vibration*, 485, 115561. <https://doi.org/10.1016/j.jsv.2020.115561>.
- Zhang, Y., Liu, Y., & Xiangl, Q. (2024). Numerical analysis of cylindrical flow control in pore-scale porous media. *Journal of Aerodynamics*, 42(6), 96-107. <https://doi.org/10.7638/kqdlxxb-2023.0148>
- Zikang, Z., & Wang, Y. (2024). Numerical simulation study of the effect of porous media passive flow control on the propulsion performance of airfoils in kármán vortex streets, *Ocean Engineering*, 311, Part 1, 118720. <https://doi.org/10.1016/j.oceaneng.2024.118720>.
- Zhou, Z., Huang, S., & Wang, Y. (2023). Numerical simulation study of the fluid-structure coupling effects of Kármán vortex street on airfoil motion with varying thickness. *Ocean Engineering*, 286, 115459. <https://doi.org/10.1016/j.oceaneng.2023.115459>.